An efficient spectral method based on an orthogonal decomposition of the velocity for transition analysis in wall bounded flow

Marc Buffat*, Lionel Le Penven, Anne Cadiou

Laboratoire de Mécanique des Fluides et d'Acoustique LMFA, Université de Lyon,
Université Claude-Bernard Lyon 1/ CNRS/ Ecole Centrale de Lyon/ Insa de Lyon
43, bd du 11 nov. 1918, 69622 Villeurbanne, FRANCE.

Abstract

As a consequence of the Helmholtz-Hodge theorem, any divergence-free vector field can be decomposed in two L^2-orthogonal, solenoidal vector fields expressed in terms of projections of the velocity and vorticity fields, on an arbitrary direction in space. Based on this type of decomposition and the choice of the wall-normal direction, an efficient spectral code is developed for incompressible flows developing between two parallel walls. The method relies on a weak formulation of the Navier-Stokes equations in the two corresponding divergence-free subspaces. The approximation is based on Fourier expansions in two directions and on the Chebyshev basis proposed by Moser et al. in the third direction in order to satisfy the wall boundary conditions. The method accuracy is validated for the plane Poiseuille linear stability problem and compared with the case of a spectral collocation method. Simulations of by-pass transition in boundary layers developing between two parallel walls are then presented. Since, by construction, the two orthogonal vector fields of the decomposition are associated respectively to the Orr-Sommerfeld and the Squire modes of the linear stability theory, the method makes it possible to evaluate kinetic energy transfers due to the coupling between these two scalar modes and their interactions with the base flow. The decomposition is also used to describe the structure of finite-length streaks in the earlier stages of transition.

Key words: Spectral method, Galerkin method, Helmholtz-Hodge decomposition, vector field decomposition, bypass transition, boundary layer, channel flow

*Corresponding author
Email addresses: `marc.buffat@univ-lyon1.fr` (Marc Buffat),
`lionel.le-penven@ec-lyon.fr` (Lionel Le Penven), `anne.cadiou@ec-lyon.fr` (Anne Cadiou)

1. Introduction

The problem of transition from laminar to turbulent flow has been the subject of intense study in the field of fluid mechanics since the pioneer work of Reynolds (1883). The challenges that have to be addressed when one wants to accurately simulate laminar-turbulent transition in fluid flow are numerous. Among other, very high accuracy of the numerical method is mandatory to obtain meaningful results (see the review in Rempfer [25]). Due to their high accuracy, spectral methods are excellent candidates to simulate transition in simple geometry, in particular with periodic boundary conditions (Gottlieb and Orszag [13], Canuto et al. [7]). Among spectral methods, pseudo-spectral/collocation methods are more popular than Galerkin/projection spectral methods because easier to formulate and implement. As pointed out by Boyd [4], the reason is simply that it is generally easier to evaluate a function than it is to integrate it. However Galerkin methods have specific advantages. They are based on variational formulations which preserve essential properties of the continuous problem such as coercivity, continuity and symmetry of the bi-linear form (Shen and Tang [29]). Besides from a numerical point of view, in time-marching problems, the matrices associated with Galerkin implicit or semi-implicit methods are banded matrices and Galerkin method are usually much faster than the collocation ones (Boyd [4]). Among Galerkin methods applied for incompressible flow solution, spectral solenoidal Galerkin or Petrov–Galerkin schemes are particularly attractive, because pressure is eliminated from the scheme by suitably projecting the equations on solenoidal subspaces (Canuto et al. [7]).

The main objective of this paper is to present a spectral projection method for incompressible flow simulation based on an orthogonal decomposition of the velocity into two solenoidal fields and to apply it for the problem of boundary layer bypass transition in a plane channel configuration. It is well-known that the linear stability problem of parallel shear flows can be formulated conveniently in terms of Orr-Sommerfeld and Squire equations, which are the two scalar differential equations for the normal velocity and vorticity components (Schmid and Henningson [28]). Correlatively, one can ask whether the normal velocity and the normal vorticity can be used to obtain an orthogonal decomposition of the velocity vector applicable to non-linear simulation of incompressible wall-bounded flows. The answer is positive and can be viewed as a consequence of the Helmholtz-Hodge decomposition theorem. Using this orthogonal decomposition, an efficient parallel spectral code has been developed for configurations of plane channel flows. The approximation is based on Fourier expansions in two directions and on the Chebyshev basis proposed by Moser et al. [22] in the third direction in order to satisfy the wall boundary conditions. The fringe technique of Bertolotti et al. [3] is used to adapt the method for the simulation of physical configurations that are not doubly-periodic.

The structure of this paper is as follows. The problem and methodology are first presented in Section 2 together with the principle of the orthogonal decomposition and its construction for periodic flows in two directions. The associated numerical method is described in Section 3. The linear stability
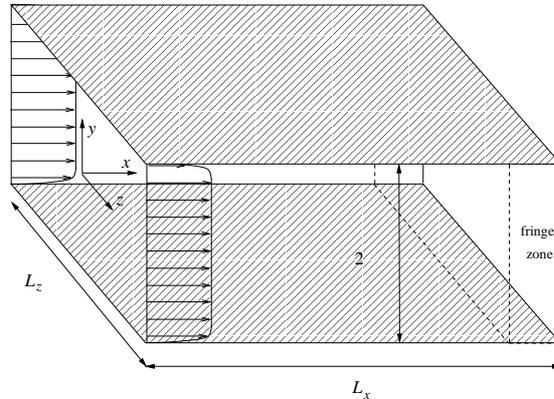
Figure 1: Computational domain Ω.

problem for the plane Poiseuille flow is first considered for validation in Section 4 and the method is compared with a spectral collocation method. Section 5 is dedicated to simulations of turbulent bypass transition in a plane channel flow, and more precisely in the entrance region where the two boundary layers are still thin compared to the channel width. For these simulations, the external perturbations are taken in the form proposed by Zaki and Durbin [31] and different amplitudes are considered. The results are similar to those presented by Zaki and Durbin [31] and Schlatter et al. [26] for a boundary layer over a flat plate. The orthogonal decomposition is used to characterize energy transfers during the first stages prior to turbulent transition, and to enlighten the structure of finite-length streaks.

2. Methodology

2.1. Governing equations

Consider an incompressible, Newtonian fluid moving between two fixed, parallel plates distant from $2h$ apart. After scaling the velocities by a constant speed U_0 and the lengths by h, the flow equations read

$$\frac{\partial \mathbf{u}}{\partial t} + \mathbf{u}.\boldsymbol{\nabla}\mathbf{u} + \boldsymbol{\nabla}p - \frac{1}{Re}\Delta\mathbf{u} = \mathbf{f} \tag{1}$$

$$\boldsymbol{\nabla}.\mathbf{u} = 0 \qquad \text{in } \Omega \tag{2}$$

where $\mathbf{u}(x, y, z, t)$ is the velocity vector, p the pressure divided by density, $Re = U_0 h/\nu$ the Reynolds number and ν the kinematic viscosity of the fluid. The computational domain considered hereafter is defined by the parallelepiped $\Omega = [0, L_x] \times [-1, 1] \times [0, L_z]$ aligned with the reference axes (x, y, z) and delimited by the walls (see Figure 1). The boundary conditions for $\mathbf{u}$ are the no-slip condition on the walls and periodicity in directions x and z. The volume force

3

f is zero except in a small region of length L_f downstream at $L_x - L_f < x < L_x$ where the following expression is used:

$$\mathbf{f} = \lambda(x)\,(\mathcal{U} - \mathbf{u}) \tag{3}$$

In this expression, $\lambda(x)$ is a smooth, positive function and $\mathcal{U}$ is a prescribed flow field. The volume force is introduced in order to simulate flows that are not naturally periodic in the x direction, while keeping the benefits of Fourier expansions in this direction. The method, due to Bertolotti et al. [3], is usually referred to as the "fringe method". In section 5, it will be applied to the case of boundary layers developing under the effect of a pressure drop between the sections $x = 0$ and $x = L_x - L_f$. By adjusting $\mathcal{U}$ so as to obtain the desired input flow at $x = 0$, the force will act downstream, in the "fringe domain", as a restoring term forcing the flow progressively to periodicity. The fringe method is analyzed in details by Nordström et al. [23].

2.2. Variational formulation

Following Pasquarelli et al. [24], the weak formulation of equations (1-2) is written in a divergence-free function space. The inner product is defined by:

$$< \mathbf{u}, \mathbf{v} >_w = \int_\Omega \mathbf{u}(x,y,z).\mathbf{v}(x,y,z)\,w(y)\,dxdydz \tag{4}$$

where $w(y)$ is a positive weight function. The space W of divergence-free trial functions and the space V of test functions are defined as follows (for conciseness the definition of the Sobolev spaces is omitted, see Pasquarelli et al. [24] for further information):

$$W = \{\mathbf{u}(x,y,z)\,\text{periodic}\,\text{in}\,(x,z)\,\text{with}\,\mathbf{u}(x,\pm1,z) = 0\,/\,\boldsymbol{\nabla}.\mathbf{u} = 0\} \tag{5}$$

$$V = \{\mathbf{v}(x,y,z)\,\text{periodic}\,\text{in}\,(x,z)\,\text{with}\,\mathbf{v}(x,\pm1,z) = 0\,/\,\boldsymbol{\nabla}.(w\,\mathbf{v}) = 0\} \tag{6}$$

The weak formulation is obtained by using the inner product of the Navier-Stokes equation (1) with a test function **v**. Using the divergence theorem, the boundary conditions and the test functions properties (6), the variational formulation equivalent to (1-2) is written:

$$\text{Find}\,\mathbf{u} \in W\,\text{such that,} \qquad \forall \mathbf{v} \in V,$$

$$< \frac{\partial \mathbf{u}}{\partial t}, \mathbf{v} >_w - \frac{1}{Re} < \Delta\mathbf{u}, \mathbf{v} >_w = \; < \mathbf{F}, \mathbf{v} >_w \tag{7}$$

$$= \; < \mathbf{f} - \boldsymbol{\nabla}p_0 + \mathbf{u} \times (\boldsymbol{\nabla} \times \mathbf{u}), \mathbf{v} >_w$$

In this expression, $\boldsymbol{\nabla}p_0$ represents the average of $\boldsymbol{\nabla}p$ over the domain Ω, and is a vector constant in space, parallel to the plane x, z. The derivation of (7) makes use of the identity $\mathbf{u}.\boldsymbol{\nabla}\mathbf{u} = \boldsymbol{\nabla}(\mathbf{u}^2/2) + (\boldsymbol{\nabla} \times \mathbf{u}) \times \mathbf{u}$. Note that the potential part of the convective acceleration, as well as the variations of the

pressure gradient, are eliminated through the projection procedure on the space of divergence-free functions W. For the generalized Stokes problem in which $\mathbf{F}$ is a given function, Pasquarelli et al. [24] prove the equivalence of (1-2) with the variational problem (7) and the uniqueness of the solution of (7).

2.3. Orthogonal decomposition of velocity field

2.3.1. A corollary to Helmholtz-Hodge decomposition theorem

Approximation methods for the solution of (7) need divergence-free basis functions in the space of solutions W. The choice of the basis functions that will be used in the following refers to a property of orthogonal decomposition of vector fields. This property is a consequence of the Helmholtz-Hodge decomposition theorem and can be stated as follows. Every square integrable, three-dimensional vector field can be split into two parts, which are orthogonal with respect to the L^2 inner product. One part is a two-dimensional, divergence-free vector field and is normal to an arbitrary chosen direction of space and the second vector field is such that its curl is normal to the specified direction. In order to satisfy orthogonality, one of the two vector fields must generally comply to some specific boundary conditions. An outline of the demonstration is now presented for the case of vector fields that are doubly periodic in the directions normal to the direction chosen for the decomposition, which is the case that will be considered in the following. It should be noted that the proposed decomposition is valid under more general conditions (Le Penven and Buffat [17]) including the fact that the domain of $\mathbf{u}$ can be bounded or not. Since the main lines of the demonstration remain the same, the following statement is kept as general as possible, except for the reference to the boundary conditions needed for orthogonality.

Let be (x, y, z) a cartesian coordinate system, $\boldsymbol{e}_x$, $\boldsymbol{e}_y$, $\boldsymbol{e}_z$, the associated unit vectors and $\nabla_\perp = (\partial_x, 0, \partial_z)^t$ the projection of the gradient operator on the plane normal to $\boldsymbol{e}_y$. Let us consider a smooth vector field and its projection $\mathbf{u}_\perp$ on the plane normal to $\mathbf{e}_y$:

$$\mathbf{u}_\perp = \mathbf{u} - (\mathbf{u}.\boldsymbol{e}_y)\boldsymbol{e}_y$$

The field $\mathbf{u}$ is supposed to be doubly periodic in (x, z) and its mean value in a plane parallel to (x, z) over a periodicity cell will be denoted as $\overline{\mathbf{u}}(y)$. Using the Helmholtz-Hodge theorem (Chorin and Marsden [8], Majda and Bertozzi [20]), this two-dimensional field can be decomposed into two doubly periodic, L^2 orthogonal fields: a two-dimensional, divergence-free vector $\mathbf{u}_{sq}$ satisfying $\overline{\mathbf{u}}_{sq}(y) = 0$ and the gradient of a scalar potential, such that:

$$\mathbf{u}_\perp = \mathbf{u}_{sq} + \nabla_\perp \phi$$

Note that the condition of zero mean value $\overline{\mathbf{u}}_{sq}(y) = 0$ is required to satisfy the orthogonality property with respect to the L^2 norm over the periodicity cell. In the general (not periodic) case, this condition would be replaced by the condition that $\mathbf{u}_{sq}$ has zero normal value on the domain of $\mathbf{u}$ (Le Penven and Buffat [17]).

5

Coming back to the initial vector field $\mathbf{u}$, the following decomposition is obtained: $\mathbf{u} = \mathbf{u}_{os} + \mathbf{u}_{sq}$ where $\mathbf{u}_{os}$ is defined by $\mathbf{u}_{os} = (\mathbf{u}.\boldsymbol{e}_y)\boldsymbol{e}_y + \boldsymbol{\nabla}_\perp \phi$. Orthogonality of $\mathbf{u}_{sq}$ and $\mathbf{u}_{os}$ is readily verified as well as the two properties mentioned in the introduction of the section: $\mathbf{u}_{sq}.\boldsymbol{e}_y = 0$ and $(\nabla \times \mathbf{u}_{os}).\boldsymbol{e}_y = 0$. Moreover, when the vector field $\mathbf{u}$ is divergence-free, the two terms of the decomposition are also divergence-free.

When the periodicity cell is simply connected, the two-dimensional solenoidal field $\mathbf{u}_{sq}$ admits a vector potential $\psi \boldsymbol{e}_y$, associated with a stream function ψ which can be chosen such that $\overline{\psi} = 0$. The potential ϕ can be split into a periodic part ϕ_1 and a linear part ϕ_0 satisfying respectively to $\overline{\phi}_1 = 0$ and $\boldsymbol{\nabla}_\perp \overline{\phi}_0 = \overline{\mathbf{u}}_\perp$. In that case, the orthogonal decomposition reads:

$$\mathbf{u} = \mathbf{u}_{os} + \mathbf{u}_{sq} \quad \text{with } \mathbf{u}_{os} = \overline{\mathbf{u}}_\perp(y) + (\mathbf{u}.\boldsymbol{e}_y)\boldsymbol{e}_y + \boldsymbol{\nabla}_\perp \phi_1, \; \mathbf{u}_{sq} = \boldsymbol{\nabla} \times \psi \boldsymbol{e}_y \quad (8)$$

Specializing to the case of solenoidal vector fields and taking the divergence and the curl of equation (8), the potential ϕ_1 and the stream function ψ are found to be the unique solutions of:

$$\nabla_\perp^2 \phi_1 = -\partial_y(\mathbf{u}.\boldsymbol{e}_y) \text{ with } \overline{\phi}_1(y) = 0, \; \nabla_\perp^2 \psi = (\boldsymbol{\nabla} \times \mathbf{u}).\boldsymbol{e}_y \text{ with } \overline{\psi}(y) = 0 \quad (9)$$

This system shows that the potential ϕ_1 is determined uniquely by the y-component of the velocity $\mathbf{u}.\boldsymbol{e}_y$, and the stream function ψ by the y-component of the curl $(\boldsymbol{\nabla} \times \mathbf{u}).\boldsymbol{e}_y$.

At this point, a justification must be given for the notation: $\mathbf{u}_{os} + \mathbf{u}_{sq}$. For parallel, incompressible flows, *i.e.* in which the velocity is expressed as $\boldsymbol{U} = U(y)\boldsymbol{e}_x$, the linear stability theory is generally formulated in terms of two scalar differential equations for the perturbation: the Orr-Sommerfeld equation for the y-component of the velocity perturbation and the Squire equation for the y-component of its vorticity (Schmid and Henningson [28]). By analogy, as they are defined respectively by the normal component of velocity and the normal component of vorticity, the two vector fields of the decomposition have been denominated as the Squire ($\mathbf{u}_{sq}$) and the Orr-Sommerfeld ($\mathbf{u}_{os}$) velocity fields.

2.3.2. Application to doubly-periodic channel flows

Coming back to the flow problem defined in Section 2.1, the decomposition $\mathbf{u} = \mathbf{u}_{os} + \mathbf{u}_{sq}$ is applied to the velocity field, solution of (7), taking $\boldsymbol{e}_y$ as the unit vector normal to the walls. In that case, the $\mathbf{u}_{os}$ velocity field (denoted by OS velocity) has zero wall-normal vorticity and its normal velocity is equal to the wall-normal velocity of $\mathbf{u}$. The $\mathbf{u}_{sq}$ vector field $\mathbf{u}_{sq}$ (denoted by SQ velocity) has zero wall-normal velocity and its wall normal vorticity is equal to the wall-normal vorticity. Moreover, its averages in the planes of constant y vanish, as required by the orthogonality condition.

Thanks to the periodicity property in x and z, an expression for $\mathbf{u}_{os}$ and $\mathbf{u}_{sq}$ can be found, using the Fourier expansion of the vector field:

$$\mathbf{u}(x, y, z, t) = \sum_{m=-\infty}^{\infty} \sum_{p=-\infty}^{\infty} \mathbf{u}^{mp}(y, t) \, e^{\imath(\alpha_m x + \beta_p z)} \quad (10)$$

where $\mathbf{u}^{mp}(y,t)$ is the complex vector of the Fourier coefficients. Equation (9) can be solved easily, and explicit expressions can be obtained for $\mathbf{u}^{mp}_{os}$ and $\mathbf{u}^{mp}_{sq}$, respectively the Fourier coefficients of the OS and SQ velocity vectors. These expressions appear as functions of $v^{mp}(y)$ and $\omega^{mp}(y)$, the Fourier components of the wall-normal velocity and wall-normal vorticity. For a non zero wave number $k = \sqrt{\alpha_m^2 + \beta_p^2}$, the OS velocity Fourier vector $\mathbf{u}^{mp}_{os}$ is obtained as

$$\mathbf{u}^{mp}_{os} = \left(\imath \, \frac{\alpha_m}{k^2} \partial_y v^{mp} \, , \, v^{mp} \, , \, \imath \, \frac{\beta_p}{k^2} \partial_y v^{mp} \right)^t \tag{11}$$

and the SQ velocity Fourier vector $\mathbf{u}^{mp}_{sq}$ by

$$\mathbf{u}^{mp}_{sq} = \left(-\imath \, \frac{\beta_p}{k^2} \omega^{mp} \, , \, 0 \, , \, \imath \, \frac{\alpha_m}{k^2} \omega^{mp} \right)^t \tag{12}$$

The Fourier coefficient for $m = n = 0$ corresponds to the contribution of the mean field $\bar{\mathbf{u}}(y)$. In that case, the decomposition is:

$$\mathbf{u}^{00}_{os} = (\bar{u}(y), \, 0, \, \bar{w}(y))^t, \ \mathbf{u}^{00}_{sq} = \mathbf{0}$$

Recalling that the Fourier coefficients of the vorticity vector are obtained by $\widehat{\boldsymbol{\nabla}} \times \mathbf{u}^{mp}$, with the operator definition $\widehat{\boldsymbol{\nabla}} = (\imath \alpha_m, \, \partial_y, \, \imath \beta_p)$, it can be noted that both velocity and vorticity Fourier vectors verify orthogonality conditions, i.e.:

$$\mathbf{u}^{mp}_{os} . \mathbf{u}^{mp}_{sq} \ = \ 0 \tag{13}$$
$$\left(\widehat{\boldsymbol{\nabla}} \times \mathbf{u}^{mp}_{os} \right) . \left(\widehat{\boldsymbol{\nabla}} \times \mathbf{u}^{mp}_{sq} \right) \ = \ 0$$

Thus, algebraic orthogonality in the Fourier space appears as the counterpart of functional orthogonality with respect to the L^2 inner product in the physical space. Again, the decomposition in the Fourier space $\mathbf{u}^{mp} = \mathbf{u}^{mp}_{os} + \mathbf{u}^{mp}_{sq}$ is unique. The OS vorticity and the SQ velocity Fourier vectors are parallel to the wall. In addition, both are orthogonal to the wave-vector $\mathbf{k} = (\alpha_m, \, 0, \, \beta_p)$, since they are solenoidal vectors fields.

Denoting by W_{mp} the function space of the Fourier coefficients $\mathbf{u}^{mp}$, the above orthogonal decomposition induces a decomposition of W_{mp} into two orthogonal subspaces W^{OS}_{mp} and W^{SQ}_{mp} spanned by vectors of the form (11) and (12) respectively.

In order to satisfy the no-slip boundary conditions at the walls, the functions $v^{mp}(y)$ and $\omega^{mp}(y)$ must verify the following conditions:

$$v^{mp}(\pm 1) = 0, \ \partial_y v^{mp}(\pm 1) = 0, \ \omega^{mp}(\pm 1) = 0 \tag{14}$$

3. Numerical method

The approximation $\mathbf{u}^h$ of the solution of equation (7) is the result of a two-step process. First, the doubly infinite Fourier sum (10) is truncated by retaining

7

only M and P components in each periodic direction. Secondly, an approximation space W_{mp}^h for each resolved Fourier coefficients $\mathbf{u}^{mp}(y,t)$ is constructed by choosing two finite sets of N trial functions $\{v_i(y)\}$ and $\{\omega_i(y)\}$ complying with the boundary conditions (14). The following approximations can be written:

$$v^{mp}(y) = \sum_{j=0}^{N-1} \alpha_{OS,j}^{mp} v_j(y), \quad \omega^{mp}(y) = \sum_{j=0}^{N-1} \alpha_{SQ,j}^{mp} \omega_j(y)$$

Using relations (11) and (12), the two associated sets of trial vectors $\{\mathbf{u}_{OS,j}^{mp}\}$ and $\{\mathbf{u}_{SQ,j}^{mp}\}$ can be defined, and the complex vector function $\mathbf{u}^{mp}(y,t)$ can then be expressed as:

$$\mathbf{u}^{mp} = \sum_{j=0}^{N-1} \alpha_{OS,j}^{mp} \mathbf{u}_{OS,j}^{mp} + \sum_{j=0}^{N-1} \alpha_{SQ,j}^{mp} \mathbf{u}_{SQ,j}^{mp} \tag{15}$$

Similarly to the definition of W_{mp}^h, the space V_{mp}^h of test functions $\mathbf{v}^{mp}$ can be defined using a comparable decomposition.

In the spaces W_{mp}^h and V_{mp}^h, the inner product associated with (4) is:

$$(\mathbf{u}^{mp}, \mathbf{v}^{mp})_w = \int_{-1}^{+1} \mathbf{u}^{mp}(y) . \overline{\mathbf{v}^{mp}(y)} \, w(y) \, dy \tag{16}$$

By denoting $\mathbf{F}^{mp}(y,t)$ the Fourier coefficients of the function $\mathbf{F}(x,y,z,t)$ introduced in (7) and by virtue of orthogonality of the trigonometric functions with respect to the inner product (4), the discrete variational formulation equivalent to (7) can be written as:

$$\forall \alpha_m, \beta_p, \ \text{find} \ \mathbf{u}^{mp} \in W_{mp}^h, \text{such that} \ \forall \mathbf{v}^{mp} \in V_{mp}^h$$
$$(\frac{\partial \mathbf{u}^{mp}}{\partial t}, \mathbf{v}^{mp})_w + \frac{1}{Re}((\alpha_m^2 + \beta_p^2)\mathbf{u}^{mp} - \partial_{yy}\mathbf{u}^{mp}, \mathbf{v}^{mp})_w = (\mathbf{F}^{mp}, \mathbf{v}^{mp})_w \tag{17}$$

Finally, by using the decomposition of the trial and test functions, two sets of differential equations are obtained for the two complex vectors of unknown coefficients $\boldsymbol{\alpha}_{OS}^{mp} = \{\alpha_{OS,j}^{mp}\}$ and $\boldsymbol{\alpha}_{SQ}^{mp} = \{\alpha_{SQ,j}^{mp}\}$:

$$\mathcal{M}_{OS}^{mp} \frac{d}{dt}(\boldsymbol{\alpha}_{OS}^{mp}) + \frac{1}{Re}(k^2 \mathcal{M}_{OS}^{mp} + \mathcal{K}_{OS}^{mp})\boldsymbol{\alpha}_{OS}^{mp} = \mathbf{b}_{OS}^{mp} \tag{18}$$
$$\mathcal{M}_{SQ}^{mp} \frac{d}{dt}(\boldsymbol{\alpha}_{SQ}^{mp}) + \frac{1}{Re}(k^2 \mathcal{M}_{SQ}^{mp} + \mathcal{K}_{SQ}^{mp})\boldsymbol{\alpha}_{SQ}^{mp} = \mathbf{b}_{SQ}^{mp}$$

where $\mathcal{M}_{OS}^{mp}$, $\mathcal{M}_{SQ}^{mp}$ and $\mathcal{K}_{OS}^{mp}$, $\mathcal{K}_{SQ}^{mp}$ are respectively the mass and rigidity matrices.

The trial functions $\{v_i(y)\}$ and $\{\omega_i(y)\}$ are defined using Chebyshev polynomials $T_i(y) = \cos[i \arccos(y)]$ known for their property to represent economically strong gradients in near-wall regions. Their expression reads, similarly to the Moser et al. [22] proposal:

$$v_j(y) = (1 - y^2)^2 \, T_j(y) \ , \ \ \omega_j(y) = (1 - y^2) \, T_j(y)$$

The polynomial prefactors are chosen so that the wall boundary conditions (14) are satisfied. The two sets of trial functions are quasi-orthogonal sets and, in order to keep the matrices sparse in (18), the Chebyshev weight function $w(y) = 1/\sqrt{(1 - y^2)}$ is used in the inner product (16). Furthermore, as they can be expressed as integrals of Chebyshev polynomials products , all the matrix coefficients are calculated exactly to avoid quadrature errors.

3.1. Stability and precision

In the case of the generalized Stokes problem (the right-hand side $\mathbf{F}$ is a given function), Pasquarelli et al. [24] proved the spectral accuracy of divergence-free spectral approximations, i.e. the convergence is $O(N^{1-s})$ for every $s \geq 1$, and more precisely:

$$\left\| \mathbf{u} - \mathbf{u}^h \right\|_\omega \leq C K_s(\mathbf{u}) \left(N^{1-s} + M^{1-s} + P^{1-s} \right) \ \ \forall s \geq 1$$

where C is a positive constant independent of N, M, P and $K_s(\mathbf{u})$ is related to the L^s norm of the velocity $\mathbf{u}$. The temporal accuracy results from the use of a second-order Crank-Nicholson/Adams Bashford scheme, that has a linear stability limit $CFL < 1$, where the CFL number is defined as:

$$CFL = \pi \, \Delta t \left(\frac{M \, |u_0|}{L_x} + \frac{N \, |v_0|}{2} + \frac{P \, |w_0|}{L_z} \right) \tag{19}$$

where (u_0, v_0, w_0) are the velocity components along x, y and z respectively and $|\ |$ is the infinity norm.

3.2. The NadiaSpectral code[1]

The method is implemented in C++ in the *NadiaSpectral* code developed at the Laboratoire de Mécanique des Fluides et d'Acoustique de l'Université de Lyon. This code is parallelized using the MPI library. The solution is advanced in time in the spectral space, using MP Fourier and $N_y = N{+}4$ Chebyshev polynomials. Taking into account the symmetries of the problem, the determination the solution at each time step needs the solution of $4MP$ real linear systems of dimension $N/2$. Evaluation of the right-hand side of (18) requires the calculation of the non-linear terms in Fourier space, i.e. convolution sums. These sums are calculated more efficiently in physical space using fast Fourier transforms. Aliasing errors from the evaluation of the nonlinear terms are removed by the 3/2-rule in the wall-parallel (x, z) plane. In the wall-normal direction y it has been found to be more convenient to increase resolution as in Schlatter

9

et al. [26]. As the linear systems can be solved independently for each couple of integers (m, p), the resolution can be efficiently parallelized on clustered computers by distributing the data along one of the two Fourier directions. However non-linear terms calculations require the use of FFT in plane (x, z), that needs data transpositions, i.e. data communications between computing nodes. As a global data transpose with MPI AlltoAll communication library functions is not very efficient, the data transposition has been optimized by distributing the data among the processors along one of the Fourier direction, the x direction for example, and by using an optimized in place point to point data transposition from (x, y) to (x, z) planes. The FFTs are performed in the (x, z) planes using real to complex 2D FFT with the optimized FFTW library of Frigo and Johnson [12]. Typical running time on parallel computer with 32 cores is 2s/time step for 14 million grid points.

The accuracy of the method is validated on the evolution of the least stable Orr-Sommerfeld eigenmode $\mathbf{U}_{crit}(y)$ in plane Poiseuille flow computed using linearized Navier-Stokes equations for $\alpha = 1$, $\beta = 0$ and $Re = U_0 h / \nu = 10000$ (the scale U_0 is the maximum of the velocity of the base flow). The calculated velocity is compared at time $t = 1$ with the one obtained from the Orr-Sommerfeld eigenfunction $\mathbf{U}_{ex} = \mathbf{U}_{crit}(y) \, e^{\imath k_x (x - \lambda_{crit} t)}$ for different spatial resolutions. Both the L^2-norm and the infinity-norm of the relative error on each velocity component are plotted on Figure 2. For both norms and both velocity components, the spectral accuracy of the method is clearly seen on this figure until the errors on the initial conditions $\mathbf{U}_{crit}(y)$ take over around 10^{-8}.

The present method has some advantages that makes it particularly efficient regarding computing cost and precision. Thanks to the projection method, each time step requires the solution of only two 1D linear systems for each wave number, instead of four when the pressure must be calculated. Using the variational formulation, the matrices of these linear systems are 5 and 7 band matrices without additional coupling lines due to the boundary conditions, as in collocation formulations. Moreover, their coefficients are calculated analytically, avoiding the cost of numerical integration and round-off errors. As it will be seen in the following, the orthogonal decomposition of the solution also allows a physical interpretation in terms of energy transfer.

4. Linear stability analysis of plane Poiseuille flow

The *NadiaSpectral* code has been validated by comparison to the linear stability analysis of the plane Poiseuille flow. The linearized Navier-Stokes equations are solved using the orthogonal decomposition and the numerical method described in Section 3. The linear systems and the associated eigenvalue problems are solved using direct factorisation and QR/QZ algorithms from the *Lapack* linear algebra package.

The spectrum for the plane Poiseuille flow at $Re = 10^4$ is shown on Figure 3a and is compared with the spectrum obtained by a spectral collocation method (*osmat* Matlab routine described in Schmid and Henningson [28]). Using the same number $N_y = 256$ of Chebyshev polynomials, the agreement
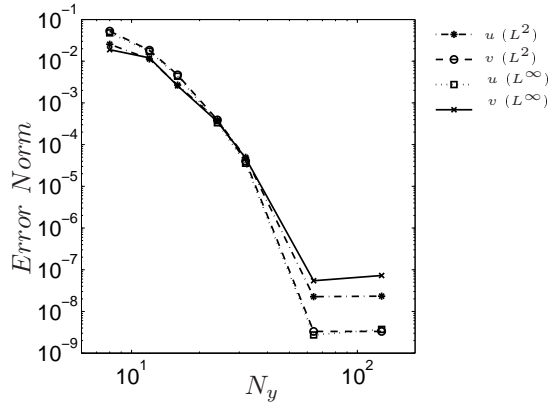
Figure 2: Relative L^2 and L^∞ error norm between the computed velocity and the Orr-Sommerfeld eigenfunction for different values of the number N_y of Chebyshev polynomials.
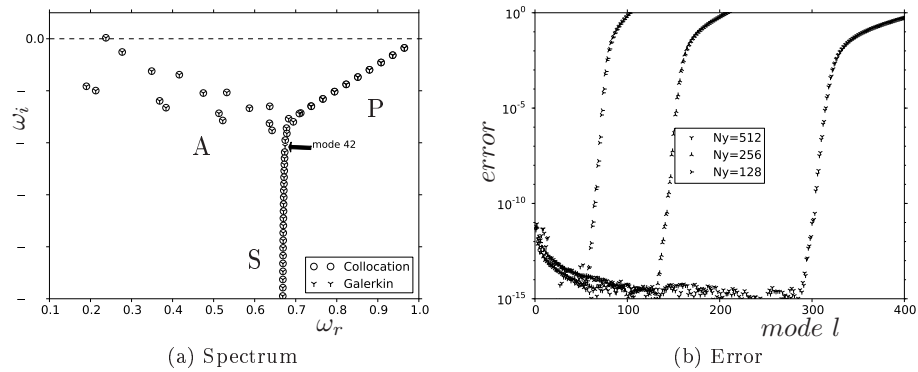
(a) Spectrum

(b) Error

Figure 3: Orr-Sommerfeld spectrum for plane Poiseuille flow at $Re = 10^4$: (a) spectrum for $\alpha = 1$ and $\beta = 0$, the three branches of the spectrum are labelled A, P, and S as suggested by Mack [19]; (b) relative error on the spectrum for $\alpha = 0$, $\beta = 1$ for different values of N_y.

is excellent and the calculated value of the only unstable complex frequency $\omega = 0.2375264887756 + 0.003739670625\,\imath$ coincides up to 10^{-12}. However it should be pointed out that the collocation method misses one eigenvalue: the mode 42 with $\omega = 0.67408 - 0.41247\,\imath$. The number of Chebyshev polynomials must be twice larger, i.e. $N_y = 512$, to obtain this mode with the collocation method.

The method accuracy is evaluated by calculating the eigenvalues for different resolutions. To do these mode-by-mode comparisons, we first consider the special case of zero streamwise wave number $\alpha = 0$, for which an analytical solution is available (Drazin and Reid [10]). Figure 3b shows the relative error for the different calculated modes and for different values of N_y. The integer l on the figure is the rank of the eigenvalue in order of decreasing imaginary part. It is seen that the first $N_y/2$ modes are well calculated within the floating point precision, whereas the last $N_y/2$ modes must be disregarded. We also check the accuracy of the calculated Orr-Sommerfeld spectrum for $\alpha = 1$ and $\beta = 0$, taking for N_y the powers of 2 from 64 to 1024. The classical Y-shape of the Poiseuille flow spectrum is obtained for the values of N_y larger than 128 (see Figure 3a, for $Re = 1000$), with a well defined vertical branch (called S-branch), corresponding to the asymptotic behaviour for the large negative values of the imaginary part of the frequency ($\omega_r = 2/3$). For the lowest value $N_y = 64$, this vertical branch cannot be observed. For all the values of N_y tested, it is noted that, at a certain point on the S-branch, corresponding roughly to a mode number $l \approx N_y/2$, the calculated eigenvalues depart from this asymptotic behaviour. After this point, the computed eigenvalues can be considered as being inaccurate. As proposed by Melenk et al. [21], the length L_S of the calculated S-branch can be taken as a measure of the numerical precision. They defined L_S as essentially the magnitude of the largest trustworthy eigenvalue and they predict its asymptotic behaviour $L_S \approx N_y^2/Re$. This asymptotic behaviour has been verified for different resolutions N_y at $Re = 10^4$. With $N_y = 512$, we found $L_S = 25.27$ which is similar to the value $L_S = 24.33$ obtained by Melenk et al. [21] with a spectral Galerkin method using Legendre polynomials of order $N = 500$. In that case the largest trustworthy eigenvalue ω_l is obtained for $l = 319$, which is close to $l \approx N_y/2$.

In order to compare with a spectral collocation method, the same validation has been done with the Matlab *osmat* code. When the number of collocation points is not high enough, some eigenvalues are missing (mode 26 for $N_y = 128$ and mode 42 for $N_y = 256$). With $N_y = 512$, all eigenvalues are predicted but the method is 100 times less accurate than the Galerkin formulation, and is also 10 times slower. Indeed Galerkin methods have the advantage of using sparse matrices and the boundary conditions are exactly satisfied. Furthermore the convergence is monotone.

5. Boundary layer transition between two parallel walls

In the last two decades, theory and computer simulations have led to significant advances in the understanding of boundary layer bypass transition induced

by free-stream disturbances (Durbin and Wu [11]). The most outstanding feature is that turbulent transition in a flat plate boundary layer can develop without the mediation of an unstable two-dimensional Tollmien-Schlichting mode. Bypass transition occurs as an instability of certain disturbances of the boundary layer that are usually designated by the name of streaks or Klebanov modes (Jacobs and Durbin [16], Brandt and Henningson [5], Brandt et al. [6]). Streaks can be described as thin jets in the streamwise direction periodically arranged in the spanwise direction. From the point of view of linear stability theory, the streaks have the property of growing transiently, although they are asymptotically stable. When the streaks have grown enough, non-linear effects, which are no longer negligible, can develop new instabilities. Streaks have been proved to be optimal structures in the sense that, in the subcritical regime, they display the highest growing rate in a finite time from all possible disturbances (Andersson et al. [1], Luchini [18]). It has also been demonstrated that they can be initiated by taking one mode from the continuous spectrum of the normal velocity equation (Orr-Sommerfeld equation). This branch of stable modes contains all the modes that are non-vanishing far from the wall and thus provides a natural basis for free-stream perturbations. These modes are strongly damped in the boundary layer, but the differences in their penetration depth has shown to have great impact on the streak growth (Zaki and Durbin [31]). In this scenario of transition, usually referred to as "bypass transition by free-steam disturbance", all the details have not yet been elucidated, in particular the spontaneous appearance of turbulent spots inside the streaky boundary layer is still not very well understood and different theories are under debate (Zaki and Durbin [31], Schlatter et al. [26]).

The present section illustrates the capability of the numerical code described in Section 3 for simulating bypass transition in boundary layers developing between two parallel walls. The approach assumes that the computational domain is far enough from the inlet section in order that the potential effect of the leading edges can be neglected and this paper only considers the case where the boundary layers are thin compared to the channel width (as described in Section 2). In the simulations, the transition in the boundary layers is forced by a free-stream perturbation consisting in two particular modes of the Orr-Sommerfeld equation following the procedure proposed by Zaki and Durbin [31].

5.1. Basis flow configuration and parameters

The computational domain Ω is the parallelepiped of Figure 1. As it will be specified in the next section, the velocity in the inlet section at $x = 0$ is virtually aligned with the x direction, its profile along y is uniform except in the two thin boundary layers close to the walls. The reference scale U_0 is taken as the mean flow velocity through the inlet section. As in (Jacobs and Durbin [16], Brandt and Henningson [5]), the flow at $x = 0$ is considered as the development of boundary layers that start at the distance x_0 upstream of the leading edges of the walls. Accordingly, we will refer to the Reynolds number, $Re_x = U_0(x + x_0)/\nu$, based on the distance from the virtual inlet section.

13

Re_h	$Re_{\delta_0^*}$	δ_0^*/h	Domain size	Resolution
20 000	344	0.017	$15h \times 2h \times 0.8h$	$728 \times 193 \times 98$

Table 1: Parameters for the presented numerical simulations.

The parameters of the simulation setup are given in Table 1. The relevant parameters are the Reynolds number, $Re_h = U_0 h/\nu$, and δ_0^*/h in which δ_0^* denotes the boundary layer displacement thickness (for each wall) at the inlet of the channel. Using the values $Re_h = 20\,000$ and $\delta_0^*/h = 0.017$, which correspond to a boundary layer thickness $\delta_{0,99}$ equal to $0.05\,h$, leads to a Reynolds number $Re_{\delta_0^*} \approx 344$, corresponding to $Re_x = 40\,000$. The computational domain height $2h$ is equal to $114\,\delta_0^*$ and its length is $15h \approx 852\,\delta_0^*$ in the streamwise direction and $0.8h \approx 45\,\delta_0^*$ in the spanwise direction. The range of Re_x values goes from $40\,000$ to $320\,000$. The extent L_f of the fringe region represents 10% of the domain size L_x.

The base flow $\boldsymbol{U}^b$ is the two-dimensional laminar flow corresponding to the development of two unperturbed symmetrical boundary layers. Since an analytical solution is not possible for $\boldsymbol{U}^b$, various approximate solutions, mostly involving Prandtl's boundary-layer approximation, have been developed for the channel flow in the inlet region (Shimomukai and Kanda [30]). Here the following approximation has been used for the base flow, including the effect of a slight increase of the free-stream velocity:

$$U^b(x,y) = U_a(x)\, f(\eta), \quad V^b(x,y) = -\int_{-h}^{y} \partial_x U^b(x,y)dy \tag{20}$$

$$\text{with } \eta = \frac{h - |y|}{\sqrt{\frac{\nu\, x}{U_a(x)}}}, \; U_a(x) = U_0\left(1 + \frac{\delta^*(x)}{h}\right) \tag{21}$$

where $f(\eta)$ is the Blasius profile and $\delta^*(x)$ the displacement thickness. At the end of the domain, the value of δ^*/h is equal to 0.0465.

5.2. Free-stream perturbation

Zaki and Durbin [31] have shown that by-pass transition in boundary layers can be initiated by only two modes of the linearized equations. These modes have zero normal vorticity and are chosen from the continuous branch of the spectrum. These so called "continuous modes" are damped significantly in the boundary layer, oscillate sinusoidally far from the wall and their phase velocity is close to the free-stream velocity when the Reynolds is large enough. They can therefore be viewed as a convenient base for the free-stream perturbations (Grosch and Salwen [14]). In Zaki-Durbin model, the first mode (mode A) has a large wavelength in the streamwise direction compared to the second one (mode B) and enters the boundary layer more deeply (Jacobs and Durbin [15]). Mode A and B are referred to as the low and the high frequency modes.

14

Perturbation	α_N	γ_N	β_N	v_{max}^N/U_0
A	$\frac{4\pi}{L_x}$	$\frac{12\pi}{h}$	$\frac{10\pi}{L_z}$	0.041, 0.029, 0.020
B	$\frac{62\pi}{L_x}$	$\frac{7\pi}{h}$	$\frac{18\pi}{L_z}$	0.021, 0.015, 0.010

Table 2: Parameters of the low-frequency ($N = A$) and high-frequency ($N = B$) perturbations used as inflow boundary conditions. Note that v_{max}^N is the maximum of the wall normal component of the velocity perturbation corresponding to three rms values $v_{rms}^d = 1.2\%, 0.9\%, 0.6\%$.

Since the normal velocity appears in the forcing term of the normal vorticity equation (Squire equation), mode A creates normal vorticity and contributes to the development of the streaks. Zaki and Durbin [31] use the mode B to perturb the streaks at the boundary layer edge and induce turbulent transition. Similar simulations have also been performed recently by Schlatter et al. [26]. For the present simulations in the channel, the perturbation has been chosen in the same way. The boundary condition for the perturbation at the entrance $\mathbf{u}^d(y, z, t)$ corresponds to the convection by the free stream of the two modes A and B:

$$\mathbf{u}^d(y, z, t) = \sum_{N=A,B} \widehat{\mathbf{u}}^N(y)\, e^{\pm \imath \alpha_N U_0 t \pm \imath \beta_N z}$$

The velocity vectors $\widehat{\mathbf{u}}^N(y)$ have zero normal vorticity and are such that their normal components are eigenmodes of Orr-Sommerfeld equation. The oscillatory behaviour of the perturbation far from the walls is characterized by a wall-normal wave number γ_N. Table 2 lists the relevant parameters of the two modes used as perturbations. The numerical values are similar to those used by Schlatter et al. [26].

Profiles of the normal component of $\widehat{\mathbf{u}}^N$ are presented on Figure 4 in the boundary layer region. As can be seen on this figure, the low-frequency perturbation A has the largest penetration depth. As explained by Durbin and Wu [11], such a perturbation gives rise to the formation of streaks in the boundary layer, whose spacing is dictated by the spanwise wave-number β_N. On the other hand, the high-frequency perturbation B does not enter deeply into the boundary layer, but its interaction with the perturbation A at the boundary layer edge can induce streak instability and then turbulent transition of the boundary layer.

5.3. Simulation results

Different simulations have been performed, with the parameters in Tables 1 and 2, using three different values of the rms value v_{rms}^d/U_0 of the wall normal velocity perturbation in the inlet section, namely 0.6%, 0.9% and 1.2%. For each case, the amplitude of perturbation B is half the amplitude of perturbation A as mentioned in Table 2. For the highest case, $v_{rms}^d = 1.2\%$, the maxima in the inlet profiles for wall normal and spanwise velocity perturbations are about 5%,

(a) mode A   (b) mode B
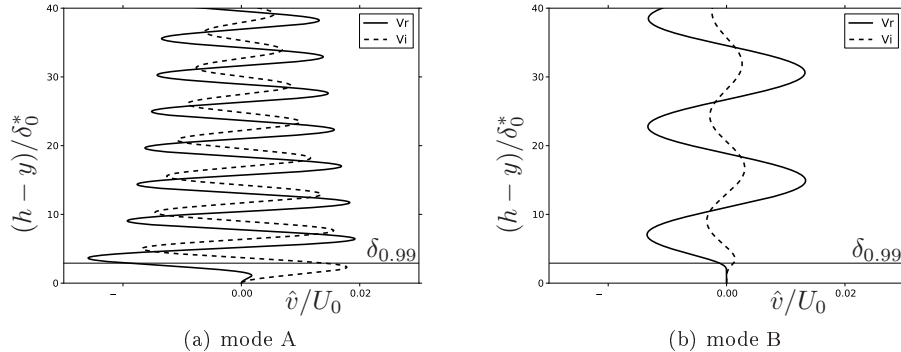
Figure 4: Wall normal component of the complex eigenfunctions $\widehat{\mathbf{u}}^N(y)$, for perturbations A and B in the case $v_{rms}^d = 0.9\%$: (a) penetrating low-frequency mode A; (b) (damped) high-frequency mode B.

whereas the streamwise maximum value is 30 times lower. Accordingly, inlet perturbations consist essentially of streamwise vortices.

5.3.1. Wall friction coefficient

The profiles of the instantaneous skin friction coefficients are plotted on Figure 5 and compared with the Blasius and turbulent correlations (Schlichting and Gersten [27]). At large time, for $v_{rms}^d = 1.2\%$ and $v_{rms}^d = 0.9\%$ the transition to the turbulent regime is observed within the computational domain. For $v_{rms}^d = 0.9\%$ the transition is observed at a larger Re_x than for $v_{rms}^d = 1.2\%$. Before the transition the friction coefficient exhibits smooth long-wave periodic surges propagating downstream and, after the transition, the profiles oscillate around the turbulent correlation with a more spiky aspect. For $v_{rms}^d = 0.6\%$ the long-wave oscillations are damped and no transition is observed within the domain. These results, showing that the highest inflow intensity case reaches a fully turbulent condition at an earlier point upstream, are similar to those found by Zaki and Durbin [32].

When the time is not large compared to the transit time in the computational box, a transient regime is observed in which turbulence is confined within a small part of the domain (see Figure 5b at time $t = 11$). These turbulent spots are now considered more particularly in order to characterize the first steps of transition and all the figures presented in the following are for time $t = 11$.

5.3.2. Kinetic energy partition of the perturbed flow

In Figure 6, the instantaneous streamwise velocity component is displayed in a plane parallel to the upper wall and located inside the boundary layer. The plot clearly shows periodic streaky patterns and downstream, except for the lowest amplitude case, more complicated structures. The periodic pattern is
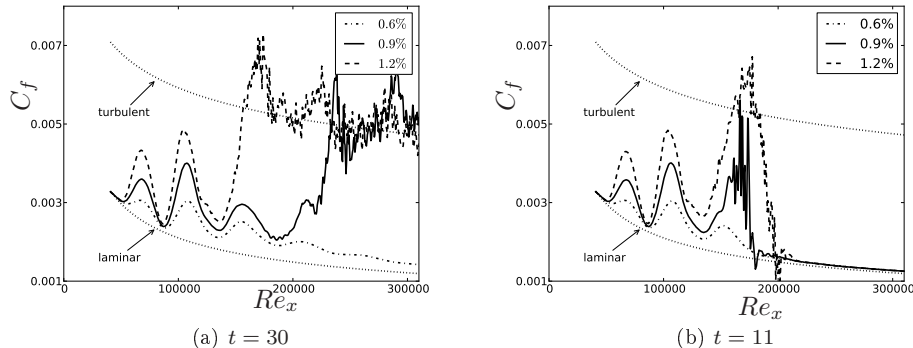
Figure 5: Skin friction coefficient C_f for different amplitudes of the inlet perturbations at two different times for $v_{rms}^d = 0.6\%$, 0.9%, 1.2%. The instantaneous C_f is spatially averaged over z on the upper channel's wall.

seen propagating with the base flow. Indeed, the rapidly-varying velocity fields downstream are associated to the turbulent spots seen on the C_f profiles. For all cases, the spanwise spacing of the streaks is equal to the spanwise wave-number of the inlet perturbation A. As it will be seen later, the particular value of the streaks size in the streamwise direction and the wavelength observed on Figure 5 are also explained by the periodic character of the inlet perturbation. In the present simulations, the streaks are not imposed as inlet boundary conditions, but appear as the result of lift-up of mean momentum by the low frequency inlet vertical perturbation v^A. This mechanism is an efficient way to generate large perturbations in the boundary layer, as seen in the present case, where inlet perturbations of 0.9% intensity induce variations on streamwise velocity that are 25 times larger. These results are very similar to those obtained for bypass transition by Zaki and Durbin [31] and Schlatter et al. [26].

To analyze the turbulent spot in the boundary layer, the perturbation field, $\mathbf{u}^p = (u^p, v^p, w^p)^t$, is defined relatively to the base flow $\boldsymbol{U}^b(x,y)$ as $\mathbf{u}^p(x,y,z,t) = \boldsymbol{U}(x,y,z,t) - \boldsymbol{U}^b(x,y)$. For the value $v_{rms}^d = 0.9\%$ at time $t = 11$, the maximum of the streamwise component u^p is about $0.6\,U_0$, which is nearly 3 times larger than the corresponding values for the other two components v^p and w^p. The iso-contour of u^p in a vertical plane corresponding to the middle of a streak is plotted on Figure 7. The regular long wavelength streak is clearly seen at the beginning of the channel on the left with alternating negative and positive velocity. A perturbation is seen on the right, which corresponds to the emergence of a turbulent spot. As seen on Figure 7, this disturbance first affects the backward perturbation jet, i.e. the region of negative streamwise velocity in the streaks, near the top of the boundary layer as suggested in Zaki and Durbin [31].

The development of a turbulent spot in the boundary layer is analyzed by

17
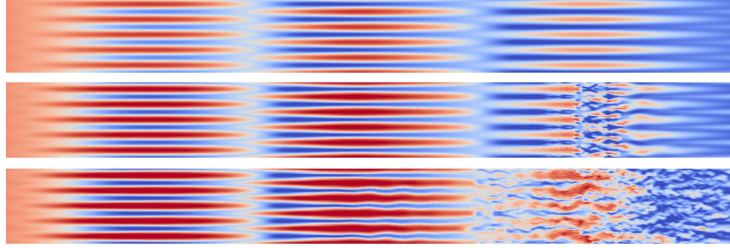
Figure 6: Top view of instantaneous streamwise velocity at fixed wall distance $2\delta_0^*$ for 3 different amplitudes of inlet perturbation, from top to bottom: $v_{rms}^d = 0.6\%$, $v_{rms}^d = 0.9\%$ and $v_{rms}^d = 1.2\%$. The range corresponds to the maximum range of the base flow with low speed streaks in blue, and high speed streaks in red. The displayed domain corresponds to the first half of the domain $0 \leq x \leq 8$, and the time is $t = 11$.

Figure 7: Instantaneous streamwise perturbation velocity u^p in a vertical plan corresponding to the middle of a streak (extrema of u^p) for $v_{rms}^d = 0.9\%$: iso-contours from blue to red corresponding to $-0.3 \leq u^p \leq 0.3$. The displayed domain corresponds to the first part of the domain $0 \leq x \leq 7$, and the time is $t = 11$.

considering averages in planes (y, z). In order to emphasize the near-wall flow, integration along y is made on the distance $\delta = 10\delta_0^*$ which is only slightly larger than the boundary layer width in the exit section (the boundary layer thickness is $\delta_{0.99} \approx 0.1\,h$ at $x = 6.5\,h$, i.e. the spot position). At a given value of x, u^δ is defined as the rms value of u^p in the channel section:

$$
u^\delta(x, t) = \sqrt{\frac{1}{\delta\,L_z} \int_{-h}^{-h+\delta} \int_0^{L_z} \left(u^p(x, y, z, t)\right)^2 \, dy \, dz} \tag{22}
$$

with similar definitions for v^δ and w^δ corresponding to v^p and w^p. The averaged kinetic energy is then defined by:

$$
E^\delta(x, t) = \frac{1}{2} \left(\left(u^\delta\right)^2 + \left(v^\delta\right)^2 + \left(w^\delta\right)^2 \right)
$$

On Figure 8, the variations of $E^\delta(x, t)$ with x clearly show that the smooth, long wavelength, oscillation attenuates in the lowest perturbation case $v_{rms}^d = 0.6\%$, whereas a transition to a more erratic dependence is seen for the highest perturbation $v_{rms}^d = 1.2\%$. For $v_{rms}^d = 0.9\%$, large perturbations are also clearly observed, but they are more localized and have smaller amplitude than for $v_{rms}^d = 1.2\%$. This behaviour is much the same as the one observed on Figure 5. As in Figure 5, the oscillations seen on the profile of E are conveyed downstream. The corresponding phase speed c_s can serve as a measure of the bulk velocity of the streaks. Moreover, since E is defined from the square of the perturbation velocity, the wavelength measured on the profiles provides an estimate of half the streamwise wavelength λ_s. As a result, the obtained values give $c_s \approx 0.55 U_0$ and c_s/λ_s is found to match well with the inlet perturbation frequency $U_0 \alpha_A / (2\pi)$.

Using the orthogonal decomposition, the results can be analyzed in terms of OS velocity $\mathbf{u}_{os}^p$ and SQ velocity $\mathbf{u}_{sq}^p$ fields. For each contribution, the near-wall rms values (such as u_{os}^δ and u_{sq}^δ for the streamwise components) are defined by expressions similar to (22). Here, the inlet perturbation is an OS velocity field, with very low streamwise component $(|u_{os}^p|/U_0 \leq 0.1\%)$. Streamwise variations of the near-wall rms values of u_{os}^p and u_{sq}^p are plotted on Figure 9 for $v_{rms}^d = 0.6\%$ (no turbulent spot) and $v_{rms}^d = 0.9\%$ (appearance of a turbulent spot). For both cases, a fast growth of the Squire streamwise velocity u_{sq}^p, whose rms value reaches 13% of U_0, is observed with the same large wavelength oscillation as seen on the energy plot (Figure 8). As already pointed out, the observed large values for the streamwise component of the SQ velocity field result from creation of normal vorticity by lift-up effect and linear interaction with the basis flow. Another observation is the fact that the Orr-Sommerfeld streamwise velocity u_{os}^p grows to quite large values, representing about 80% of u_{sq}^p for the higher value of v_{rms}^d. In this case, the OS velocity field and the SQ velocity field contribute to the jet-like structure of the streaks with almost equal importance. In contrast to the linear growth of u_{sq}^p, this increase of u_{os}^p is related to a nonlinear mechanism, and will be discussed below. For
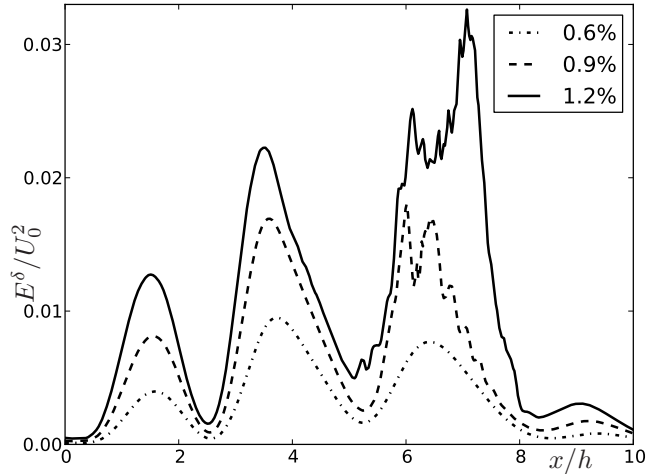
Figure 8: Evolution of averaged value of kinetic energy $E^\delta(x,t)$ in the upper boundary layer at time $t = 11$, for 3 different amplitudes of the perturbations.

the lowest perturbation $v_{rms}^d = 0.6\%$, after the growing phase, the SQ and the OS velocity fields are damped by viscosity and no transition is observed. For $v_{rms}^d = 0.9\%$, the strong high wave-number oscillations seen on the energy profile near $x \approx 6h$ are observed on both contributions u_{os}^p and u_{sq}^p. The near-wall rms values v_{os}^δ, v_{sq}^δ and w_{os}^δ, w_{sq}^δ, for the wall-normal and the spanwise perturbation respectively, are 10 times smaller than the values for the streamwise component in the streaks region, but they grow rapidly in the spot region to reach 40% of u_{sq}^δ. As expected, the streaks are essentially one dimensional streamwise jet-like perturbations, and the perturbations become three-dimensional in the spot region.

5.3.3. Orthogonal decomposition of the streak patterns

Instantaneous contours of streamwise velocity perturbation are plotted on Figures 11 and 10 together with the two contributions resulting from the or-thogonal decomposition. In the streaks region, the plane SQ velocity field $\mathbf{u}_{sq}^p$ (upper plot in Figures 11 and 10a) is a regular set of vortices orthogonal to the wall, elongated in the streamwise direction. The contribution of these vortices can be easily identified in the total streamwise velocity perturbation u^p (lower plot on Figure 10a). The OS velocity field $\mathbf{u}_{os}^p$ (lower plot on Figure 11 and middle plot on Figure 10a) is a two-dimensional field, constant in the spanwise direction, consisting of spanwise vortices elongated in the streamwise direction. With negative values of u_{os}^p at the edge and positive values in the near-wall region, these vortices reinforce the forward SQ perturbation velocity u_{sq}^p in the near-wall region and the backward SQ perturbation velocity u_{sq}^p at the edge of

20
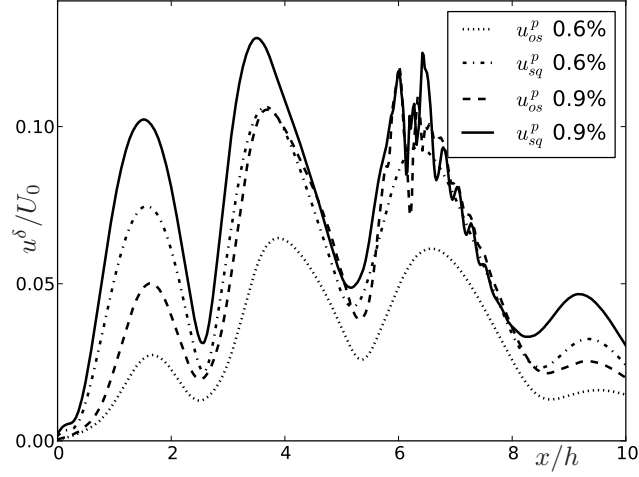
Figure 9: Near-wall rms values of streamwise velocity perturbation, u_{os}^δ and u_{sq}^δ, for 2 different amplitudes of inlet perturbation.

(a) $x = 4h$ (b) $x = 6.9h$
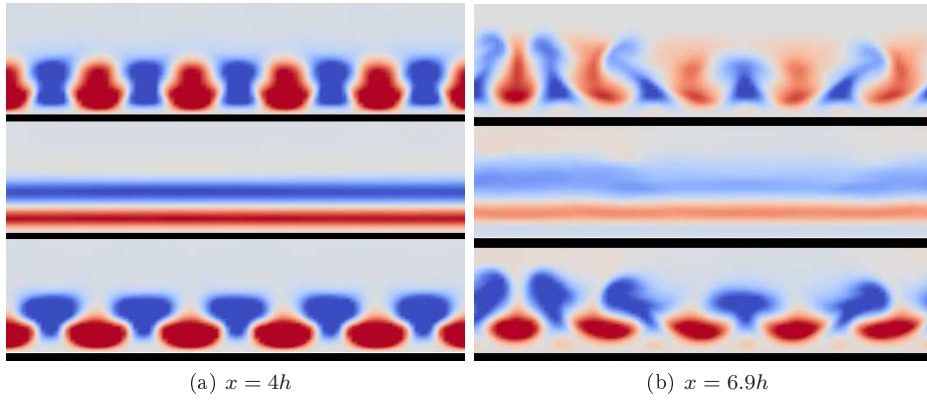
Figure 10: Instantaneous contours of streamwise velocity perturbation ($-0.3 \leq u^p \leq 0.3$) for $v_{rms}^d = 0.9\%$ displayed using the orthogonal decomposition in two cross sections: (a) in the streaks region and (b) near the turbulent burst. From top to bottom: SQ velocity u_{sq}^p, OS velocity u_{os}^p, total perturbation $u^p = u_{os}^p + u_{sq}^p$.

Figure 11: Instantaneous contours of streamwise velocity perturbation ($-0.3 \leq u^p \leq 0.3$) for $v_{rms}^d = 0.9\%$ displayed using the orthogonal decomposition: (top) SQ velocity u_{sq}^p in an horizontal plane at fixed wall distance $2\delta_0^*$; (bottom) OS velocity u_{os}^p in a vertical plane.

the boundary layer, as seen on the lower plot of Figure 10a. Noting that the SQ has nearly zero average in the spanwise direction, one can consider that, in the streaks region, the OS velocity field $\mathbf{u}_{os}^p$ and the SQ velocity field $\mathbf{u}_{sq}^p$ represent the spanwise-averaged part and the spanwise-varying part of the perturbation $\mathbf{u}^p$, respectively. The spatial structure of both terms is sketched in Figure 12.

The SQ velocity $\mathbf{u}_{sq}^p$ mainly results from linear forcing in the Squire equation by the low-frequency perturbation A (α_A, β_A). It has the same spanwise wavelength $2\pi/\beta_A$ as the inlet perturbation A and its streamwise wavelength λ_s is related to the inlet temporal frequency $f_A = \alpha_A U_0/2\pi$ as seen before. By contrast, the OS velocity $\mathbf{u}_{os}^p$ is essentially due to non-linear interactions. The OS velocity field plotted in Figure 12 shows a periodic row of vortices oriented in the streamwise direction at twice the streaks frequency. The corotative character of the vortices is an indication that the spatial spectrum of the OS vector field has a large contribution at zero frequency in addition to the pure sinusoidal one. These two contributions can be explained by quadratic interactions between the four modes ($\pm\alpha_A, \pm\beta_A$) defining the inlet perturbation A. Energy transfer to mode ($2\alpha_A, 0$) can be explained by quadratic interactions between modes (α_A, β_A) and ($\alpha_A, -\beta_A$). On the other hand, the continuous contribution is explained by interactions between modes (α_A, β_A) and ($-\alpha_A, -\beta_A$). Energy levels of these two modes of $\mathbf{u}_{os}^p$ are similar, and the total energy of $\mathbf{u}_{os}^p$ represents 64% of the energy of $\mathbf{u}_{sq}^p$.

In the transition region, strong oscillations of the streaks are observed in the spanwise direction. In that region, the plot of the streamwise perturbation $\mathbf{u}^p$ (lower plot on Figure 10b) clearly shows spanwise oscillations of the low speed streaks on top of the boundary layer. Figure 10b shows that the instability mainly affects the SQ streamwise velocity u_{sq}^p, whereas the OS streamwise velocity u_{os}^p remains almost unaffected. These oscillations are also visible on rms values of u_{sq}^p (Figure 9) upstream of the spot. They are found to move downstream at the streaks velocity c_s and their time frequency is in agreement with the frequency of the inflow mode B. At the early stage, before breakdown, this instability occurs through perturbations of the SQ streamwise velocity u_{sq}^p and looks very similar to the transverse instabilities studied by Andersson et al. [2].

The question naturally emerges of whether and how the OS velocity field
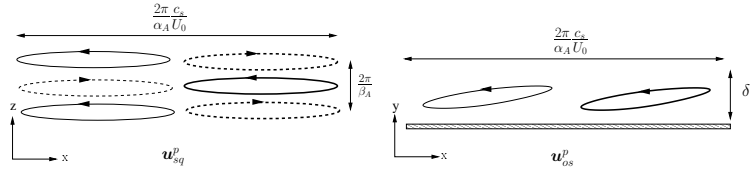
Figure 12: Sketch of the orthogonal decomposition in the streaks region: the SQ velocity $\mathbf{u}_{sq}^p$ (on the left) is the spanwise varying part of the perturbation field, corresponding to the linear response associated with a mode (α_A, β_A); the OS velocity field $\mathbf{u}_{os}^p$ (on the right) is the spanwise-averaged part of the perturbation field corresponding to the non linear response associated with modes $(2\alpha_A, 0)$ and $(0,0)$.

$\mathbf{u}_{os}^p$ acts on the stability of the streaks. If α_A was taken equal to zero, the two modal contribution to $\mathbf{u}_{os}^p$ would merge and the effect of $\mathbf{u}_{os}^p$ would be viewed simply as a change in the dependence of the base flow with respect to the wall normal coordinate. In this situation, that corresponds to steady (or infinite) streaks, it has been clearly demonstrated that non-linear distortion of the base flow has important effects on the stability of the streaks. For streaks of moderate amplitude, Cossu and Brandt [9] have shown that it tends to stabilize the Blasius profile with respect to Tollmien-Schlichting waves. For streaks of larger amplitude capable of causing inflectional instability, Andersson et al. [2] have shown that the instability thresholds, and also the nature of the most unstable mode, are very different whether the non-linear field is considered or not. The location of the turbulent spots inside the streaks of finite length remains also an open question. In the present simulations, the turbulent spot appears in the downstream part of the perturbed streaks, where the OS streamwise velocity u_{os}^p has larger values. A stability analysis of streaks of finite length, taking into account the streamwise variations of the non-linear distortion of the base profile, should be performed to answer these questions.

6. Conclusion

This paper presents numerical simulations of boundary layer transition in a plane channel flow. The numerical method is based on the spectral projection on two orthogonal, divergence-free subspaces. Fourier-Chebyshev expansions are used and, more specifically, the Chebyshev basis proposed by Moser et al. [22] in order to satisfy the wall boundary conditions. To simulate non-periodic flows, the fringe technique introduced by Bertolotti et al. [3] is employed. An interesting feature of the method is the direct access to two solenoidal vector fields that play special roles in the early stages of turbulent transition and, also, the possibility to quantify energy transfers between them. Another characteristic is the use of a projection on divergence-free subspaces, ensuring that the solution field remains solenoidal, whatever are the forcing terms in the equations.

This allows a robust and accurate implementation of non-periodic boundary conditions using the fringe method.

The approach is first validated on the classical stability analysis of the plane Poiseuille flow. The results illustrate the accuracy of the present spectral projection method, which allows to obtain the spectrum precisely without missing eigenvalues. Then, the method is applied to the study of turbulent transition in the boundary layers developing in a plane channel flow. The considered case corresponds to a large Reynolds number flow and is such that the transition occurs while the boundary layers are still thin compared to the channel width. Without external perturbations, the flow remains laminar and the classical Blasius skin friction coefficient is recovered. By-pass transition is induced in the boundary layers by external vortical disturbances using a model similar to the one proposed by Zaki and Durbin [31]. As the boundary layer thickness is small compared to the channel height, similar results are obtained to those presented by Zaki and Durbin [31] and Schlatter et al. [26] for a boundary layer over a flat plate. Using the orthogonal decomposition of the velocity, specific information about the structure of streaks of finite length is given. Specifically, the streaks are found as the sum of two L^2-orthogonal contributions, one part is the SQ velocity field $\mathbf{u}_{sq}^p$, which is a streamwise oriented contribution representing 60% of the total kinetic energy, the other part is the OS velocity field $\mathbf{u}_{os}^p$ which is a spanwise invariant term with 40% of the kinetic energy. In the early steps of the transition, the secondary instability affects mainly the SQ streamwise velocity u_{sq}^p, whereas the OS streamwise velocity u_{os}^p remains almost unaffected.

Acknowledgments

References

[1] Andersson, P., Berggren, M., Henningson, D. S., 1999. Optimal disturbances and bypass transition in boundary layers. Phys. Fluids 11, 134–150.

[2] Andersson, P., Brandt, L., Bottaro, A., Henningson, D. S., 2001. On the breakdown of boundary layers streaks. J. Fluid Mech. 428, 29–60.

[3] Bertolotti, F. P., Herbert, T., Spalart, P. R., 1992. Linear and nonlinear stability of the Blasius boundary layer. J. Fluid Mech. 242, 441–474.

---

[2]`http://www.flchp.univ-lyon1.fr`

[4] Boyd, J. P., 2001. Chebyshev and Fourier spectral methods. Courier Dover Publications.

[5] Brandt, L., Henningson, D., 2002. Transition of streamwise streaks in zero-pressure-gradient boundary layers. J. Fluid Mech. 472, 229–262.

[6] Brandt, L., Schlatter, P., Henningson, D. S., 2004. Transition in boundary layers subject to free-stream turbulence. Journal of Fluid Mechanics 517, 167–198.

[7] Canuto, C., Hussaini, M., Quarteroni, A., Zang, T., 1988. Spectral Methods in Fluid Dynamics. Springer-Verlag, New York.

[8] Chorin, A. J., Marsden, J. E., 2000. A mathematical introduction to fluid mechanics. Springer.

[9] Cossu, C., Brandt, L., 2002. Stabilization of tollmien-schlichting waves by finite amplitude optimal streaks in the Blasius boundary layer. Phys. Fluids 14, L57–60.

[10] Drazin, P. G., Reid, W. H., 2004. Hydrodynamic Stability. Cambridge University Press.

[11] Durbin, P., Wu, X., 2007. Transition beneath vortical disturbances. Annual Review of Fluid Mechanics 39, 107–128.

[12] Frigo, M., Johnson, S. G., 2005. The design and implementation of fftw3. In: Proceedings of the IEEE 93, Special Issue on Program Generation, Optimization, and Platform Adaptation. No. 93 in 2. pp. 216–231.

[13] Gottlieb, D., Orszag, S. A., 1977. Numerical analysis of spectral methods: Theory and Applications. NSF-CBMS Monograph No. 26. SIAM.

[14] Grosch, C. E., Salwen, H., 1978. The continuous spectrum of the orr-sommerfed equation. part 1. the spectrum and the eigenfunctions. Journal of Fluid Mechanics 87, 1, 33–54.

[15] Jacobs, R. G., Durbin, P. A., 1998. Shear sheltering and the continuous spectrum of the orr-sommerfeld equation. Phys. Fluids 10 (8), 2006–2011.

[16] Jacobs, R. G., Durbin, P. A., 2001. Simulations of bypass transition. J. Fluid Mech 428, 185–212.

[17] Le Penven, L., Buffat, M., 2009. An orthogonal decomposition of soleinoidal fields function of the normal velocity and normal vorticity components. Tech. rep., Laboratoire de Mécanique des Fluides et Acoustique LMFA, Université de Lyon.

[18] Luchini, P., 2000. Reynolds-number-independent instability of the boundary layer over a flat surface: optimal perturbations. J. Fluid Mech. 404, 289–309.

[19] Mack, L. M., 1976. A numerical study of the temporal eigenvalue spectrum of the Blasius boundary layer. J. Fluid Mech. 73, 497–520.

[20] Majda, A. J., Bertozzi, A. L., 2002. Vorticity and incompressible flow. Cambridge University Press.

[21] Melenk, J., Kirchner, N., Schwab, C., 2000. Spectral Galerkin discretization for hydrodynamic stability problems. Computing 65, 97–118.

[22] Moser, R. D., Moin, P., Leonard, A., 1983. A spectral numerical method for the Navier-Stokes equations with applications to Taylor-Couette flow. J. Comp. Phys. 52, 524–544.

[23] Nordström, J., Nordin, N., Henningson, D., 1999. The fringe region technique and the Fourier method used in the direct numerical. SIAM Journal on Scientific Computing 20, 1365–1393.

[24] Pasquarelli, F., Quarteroni, A., Sacchi-Landriani, G., 1987. Spectral approximations of the Stokes problem by divergence-free functions. Journal of Scientific Computing 2, 1995–2026.

[25] Rempfer, D., 2003. Low-dimensional modeling and numerical simulation of transition in simple shear flows. Annu. Rev. Fluid Mech. 35, 229–65.

[26] Schlatter, P., Brandt, L., de Lange, H. C., Henningson, D. S., 2008. On streak breakdown in bypass transition. Physics of Fluids 20, 101205.

[27] Schlichting, H., Gersten, K., 2000. Boundary-layer theory, 8th Edition. Springer.

[28] Schmid, P. J., Henningson, D. S., 2001. Stability and Transition in Shear Flows. Springer.

[29] Shen, J., Tang, T., 2006. Spectral and High-Order Methods with Applications. Science Press of China.

[30] Shimomukai, K., Kanda, H., 2006. Numerical study of normal pressure distribution in entrance flow between parallel plates: finite difference calculations. Electronic Transactions on Numerical Analysis 23, 202–218.

[31] Zaki, T. A., Durbin, P. A., 2005. Mode interaction and the bypass route to transition. Journal of Fluid Mechanics 85-111.

[32] Zaki, T. A., Durbin, P. A., 2006. Continuous mode transition and the effects of pressure gradient. J. Fluid Mechanics 563, 357–388.